Energy & Environmental Science

Cite this: *Energy Environ. Sci.*, 2012, **5**, 7066

www.rsc.org/ees

PAPER

An intermediate-temperature solid oxide fuel cell with electrospun nanofiber cathode†

Mingjia Zhi,[ab] Shiwoo Lee,[a] Nicholas Miller,[ac] Norbert H. Menzler[d] and Nianqiang Wu*[ab]

Received 8th September 2011, Accepted 27th February 2012
DOI: 10.1039/c2ee02619h

Lanthanum strontium cobalt ferrite (LSCF) nanofibers have been fabricated by the electrospinning method and used as the cathode of an intermediate-temperature solid oxide fuel cell (SOFC) with yttria-stabilized zirconia (YSZ) electrolyte. The three-dimensional nanofiber network cathode has several advantages: (i) high porosity; (ii) high percolation; (iii) continuous pathway for charge transport; (iv) good thermal stability at the operating temperature; and (v) excellent scaffold for infiltration. The fuel cell with the monolithic LSCF nanofiber cathode exhibits a power density of 0.90 W cm^{-2} at 1.9 A cm^{-2} at 750 °C. The electrochemical performance of the fuel cell has been further improved by infiltration of 20 wt% of gadolinia-doped ceria (GDC) into the LSCF nanofiber cathode. The fuel cell with the LSCF–20% GDC composite cathode shows a power density of 1.07 W cm^{-2} at 1.9 A cm^{-2} at 750 °C. The results obtained show that one-dimensional nanostructures such as nanofibers hold great promise as electrode materials for intermediate-temperature SOFCs.

1. Introduction

Solid oxide fuel cells (SOFCs) based on yttria-stabilized zirconia (YSZ) electrolyte typically are operated at high temperature (850–1000 °C).[1–4] Such a high operating temperature not only restricts the material selection for the stack components such as interconnect and sealing but also causes instability of thermal cycling. Therefore there is a strong incentive to develop SOFCs that are operated at intermediate temperature (600–750 °C) with an acceptable power density.[5–7] However, the performance of YSZ-based SOFCs deteriorates with a decrease in operating temperature since the polarization resistance at the cathode increases remarkably. Numerous efforts have been made to develop new materials and/or architectures for SOFC cathodes operated at intermediate temperature.[8–13] A new class of ferrite-based mixed ionic–electronic conductor (MIEC) materials has been developed to fulfil such a need.[14] Incorporation of nanomaterials into the cathode is an alternative solution. Zero-dimensional (0-D) nanomaterials (called nanoparticles) have large surface-to-volume ratio and enhanced electrocatalytic activity but poor thermal stability.[15,16] We recently introduced one-dimensional (1-D) nanomaterials such as nanofibers into SOFC cathodes[17] since 1-D nanomaterials have not only large surface-to-volume ratio[18] and high catalytic activity,[17] but also high charge mobility[19] and good thermal stability.[17] Our results obtained from a half-cell test show that the ionic YSZ nanofibers facilitate the oxygen reduction reaction at the SOFC cathode.[17]

[a]*National Energy Technology Laboratory, Department of Energy, 3610 Collins Ferry Road, Morgantown, WV, 26507, USA*
[b]*Department of Mechanical and Aerospace Engineering, WVNano Initiative, West Virginia University, Morgantown, WV 26506-6106, USA. E-mail: nick.wu@mail.wvu.edu; Fax: +1-(304)-293-6689; Tel: +1-(304)-293-3326*
[c]*URS Corporation, Morgantown, WV, 26507, USA*
[d]*Institute of Energy and Climate Research, IEK-1 Forschungszentrum, Jülich GmbH, 52425 Jülich, Germany*
† Electronic supplementary information (ESI) available: Fig. S1–S6 and Table S1. See DOI: 10.1039/c2ee02619h

Broader context

A solid oxide fuel cell (SOFC) is an electrochemical device that generates clean, highly efficient power onsite from a wide range of fuel sources. Conventional SOFCs based on yttria-stabilized zirconia (YSZ) electrolyte require an operating temperature of over 800 °C. Reduction of operating temperature below 800 °C will significantly extend the lifetime, provide better flexibility in materials selection, and reduce the cost. A three-dimensional porous nanofiber network structure has been developed as a SOFC cathode, which results in a high-power-density SOFC operated at 750 °C. This work has shown that the performance of the SOFC can be enhanced by designing and tailoring the electrode architecture on the nanoscale. The knowledge obtained will have implications in development of low-cost, high-efficiency SOFCs operated at intermediate temperature.

In the present work, a MIEC material composed of lanthanum strontium cobalt ferrite (LSCF) nanofibers was synthesized for SOFC cathode application by a high-yield electrospinning method. It is postulated that the 1-D LSCF nanofibers will provide continuous pathways for both electrons and oxygen ions throughout the whole cathode. The stacking of such nanofibers will form a highly porous network structure, which is expected to facilitate the transport of gas molecules. Furthermore, the infiltration of ionic gadolinium-doped ceria (GDC) into the LSCF nanofiber network will be explored to further improve the cathode performance.

2. Experimental

2.1 Synthesis of nanofibers

Polyacrylonitrile (PAN; 6 wt%) was dissolved in *N*,*N*-dimethylformamide (DMF) at 60 °C under stirring until a clear yellow solution was formed. $La(CH_3COO)_3 \cdot 1.5H_2O$, $Sr(CH_3COO)_2 \cdot 0.5H_2O$, $Co(CH_3COO)_2 \cdot 4H_2O$, and $Fe(CH_3COO)_2$ were then added into the solution at a molar ratio of 0.58 : 0.4 : 0.2 : 0.8 in order to yield $La_{0.58}Sr_{0.4}Co_{0.2}Fe_{0.8}O_3$. The solution was stirred at 80 °C until complete dissolution. The recipe was expected to generate slight A-site-deficient perovskite-structured ABO_3 based on the literature.[20] The precursor was then loaded into a syringe mounted on a syringe pump. The electrospinning experiment was conducted at an electrical field of 1.2 kV cm^{-1} at an injection rate of 0.25 ml h^{-1}. A grounded stainless steel foil was used as the collector of the electrospun nanofibers. The as-spun nanofiber mats were then peeled off from the collector after heat-treatment at 800 °C to achieve the perovskite phase.

2.2 Fabrication and testing of fuel cells

The anode-supported half-cells were supplied by Forschungszentrum Jülich (Germany). The cell dimension was 23 mm × 23 mm. The four-layer structure included a 500 μm thick NiO–YSZ anode-support layer fabricated by tape-casting, an 8 μm thin anode layer composed of NiO–YSZ, a 10 μm thick YSZ electrolyte layer, and a 7 μm thick GDC buffer layer, which was intended to prevent the possible reaction between LSCF and YSZ. All functional layers were applied by screen printing and firing at adjusted temperatures.[21,22] The raw materials used were 8YSZ (TZ-8Y, Tosoh Company, Japan) for the anode and the electrolyte, 8YSZ (UCM Company, Germany) for the thick support, NiO (Mallinckrodt Baker, Germany) for the support and the anode, and GDC (Treibacher, Austria) for the buffer layer. The LSCF nanofibers were pasted on the half-cell after they had been ground with a commercial ink vehicle (IV, Nextech Materials) at a mass ratio of 1 : 5. The fuel cell was then heated at 925 °C for 3 h at a rate of 1 °C min^{-1} to sinter the cathode. The active cathode area was 1 cm × 1 cm in a square, which was used for calculation of the power density. The cathode mass was determined by measuring the difference in the weight of the cell before and after cathode sintering. This type of fuel cell is denoted in the following as LSCF NF.

To infiltrate GDC into the LSCF cathode, a precursor was prepared by dissolving 6 wt% of PAN, 0.4 M $Ce(NO_3)_3$, and 0.1 M $Gd(NO_3)_3$ in DMF. The precursor was then applied to the cathode using a precise pipette. The average LSCF loading was ~6 mg cm^{-2} and the applied GDC precursor was 15–60 μl cm^{-2} depending on the design. The electrodes were then fired at 800 °C for 1 h at a rate of 1 °C min^{-1}. Cathodes in a mass ratio of 20% GDC : 80% LSCF and 50% GDC : 50% LSCF were fabricated, which are denoted in the following as LSCF20GDC and LSCF50GDC, respectively.

Fig. 1 shows the configuration for fuel cell testing. The fuel cell was mounted at the end of a zirconia tube and sealed by Aremco Ceramabond 552 on the edge. Dry air was supplied to the SOFC cathode side and 3% H_2O humidified H_2 was used as the fuel at the anode side. The area of the anode exposed to H_2 was 1.25 cm^2. The flow rate was 200 sccm (standard cubic centimetres per minute) for both sides. Silver paste and silver mesh were used as the current collector. The cells were connected to a Solartron 1260 potentiostat/1287 impedance analyzer using silver wires for electrochemical characterization from 600 °C to 800 °C with an interval of 50 °C. The impedance spectra were recorded in the AC frequency range from 30 kHz to 0.1 Hz with an AC amplitude of 10 mV at open circuit. The cell *V*–*I* curves were obtained by loading the cell up to 2 A cm^{-2} at a rate of 10 mA s^{-1}.

2.3 Characterization of materials

The morphologies of the nanofibers and the SOFC cathodes were examined using Hitachi S-4000 and JEOL JSM7600F scanning electron microscopy (SEM) instruments equipped with energy dispersive X-ray spectroscopy (EDX) capability. A thin gold film was deposited prior to SEM observation. The crystalline phase was determined by X-ray diffraction (XRD) using a Panalytical X-ray diffractometer. The crystal structure of individual nanofibers was examined by transmission electron microscopy (TEM; FEI/Philips CM20) and select area electron diffraction (SAED).

3. Results and discussion

Fig. 2 shows the SEM images of the LSCF nanofibers after calcination at 800 °C. The nanofibers were up to several hundred microns long and formed a porous network (Fig. 2(a)). The distribution of the nanofiber diameter was estimated based on the data obtained from 100 nanofibers (Fig. 2(c)). The median value of the diameter was 230 nm. XRD analysis shows that all

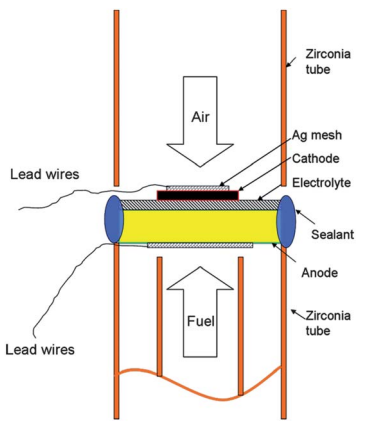

Fig. 1 Illustration of fuel cell testing.

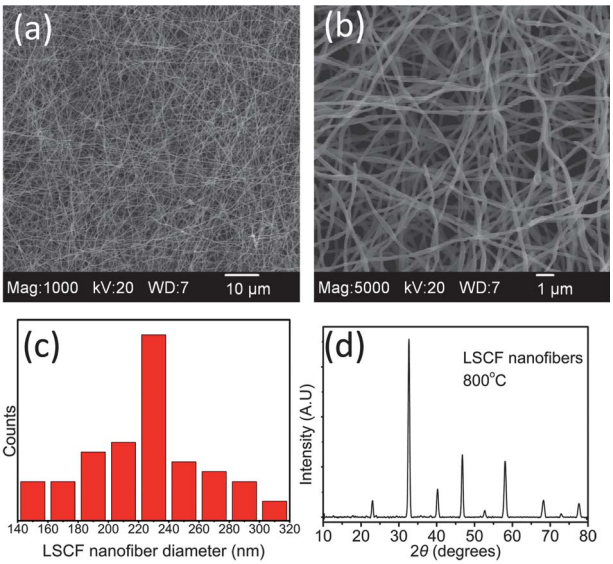

Fig. 2 SEM images of the electrospun LSCF nanofibers after calcination at 800 °C: (a) low magnification; (b) high magnification. (c) Diameter distribution of the nanofibers. (d) XRD pattern of the nanofibers.

the peaks of the pattern were consistent with the JCPDS data of rhombohedral LSCF (Fig. 2(d)). The average grain size of the rhombohedral LSCF phase was calculated according to Scherrer's equation:

$$D = \frac{0.9\lambda}{B \times \cos\theta} \quad (1)$$

where D is the grain size, λ is the wavelength of the X-rays (0.154 nm), B is the peak width at the half-maximum intensity, and θ is the diffraction angle. The grain size was calculated to be ~45 nm. It should be noted that the fibers used in this study had a much smaller diameter as compared to LSM fibers fabricated by an extrusion method (fiber diameter: 40–150 microns).[23] Ultrafine fibers are desirable for the SOFC electrode.[23]

TEM was used to further confirm the morphology and structure of the LSCF nanofibers. Fig. 3(a) shows the bright-field TEM image of a single LSCF nanofiber and the corresponding SAED pattern. The diameter of the nanofiber was around 200 nm and the crystal structure was confirmed to be perovskite from the SAED pattern. It can be seen that the nanofiber was composed of nanograins with grain size of about 50 nm. The nanograin size was consistent with the data derived from the XRD pattern. The nanograins were connected with each other intimately. The EDX spectrum reveals that the nanofiber contained La, Sr, Fe, and Co as shown in Fig. 3(b).

Fig. 4(a) shows the morphology of the LSCF cathode after the nanofibers had been deposited on the electrolyte and sintered. The fibrous network structure was retained. The mean diameter of the nanofiber became around 240 nm, which was slightly larger than that of the raw fibers before sintering. Large pores at the micron scale were observed within the nanofiber network. Fig. 4(b) shows the cross-section of the fuel cell on the cathode side. It can be seen that the cathode was about 40 μm thick. Given the LSCF loading of ~6 mg cm^{-2}, the porosity of the cathode (P) was estimated as

$$P = 1 - \frac{m}{A \times T \times \rho} \quad (2)$$

where m is the cathode mass, A and T are the cathode area and thickness, and ρ is the theoretical density of LSCF (~6 g cm^{-3}). The calculated cathode porosity was estimated to be 75%. This reveals that a highly porous cathode was successfully fabricated without addition of any filler. It can also be seen from Fig. 4(b) that a good contact was formed between the LSCF nanofiber and the GDC buffer layer, which is important to the cell performance.

Fig. 5(a) demonstrates the V–I curves of the fuel cell with the LSCF nanofiber cathode that was operated in the range of 600 °C to 800 °C. The open circuit voltages were 1.12 V and 1.05 V at 600 °C and 800 °C, respectively, which indicated a dense electrolyte as well as good sealing in the test apparatus. The cell yielded a power density of 0.27 W cm^{-2} at a current density of 0.5 A cm^{-2} at 600 °C, which increased to 1.22 W cm^{-2}

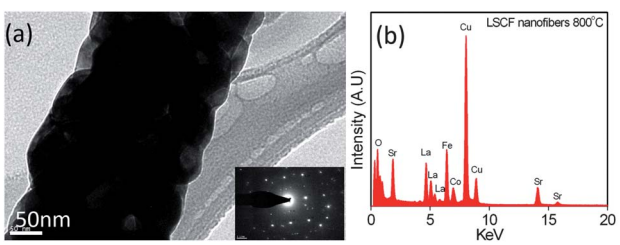

Fig. 3 (a) TEM image of single electrospun LSCF nanofiber after calcination at 800 °C; the inset shows the corresponding SAED pattern. (b) EDX spectrum taken from the nanofiber (the Cu signal came from the Cu grid).

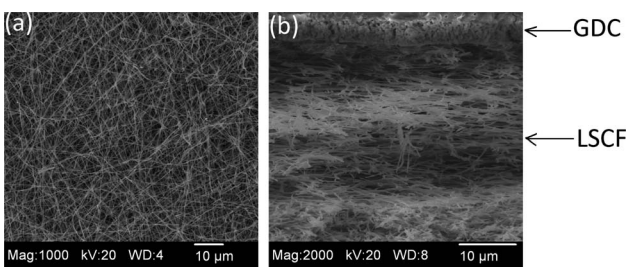

Fig. 4 SEM images of the LSCF nanofiber cathode: (a) top view of the cathode and (b) cross-section of the cathode.

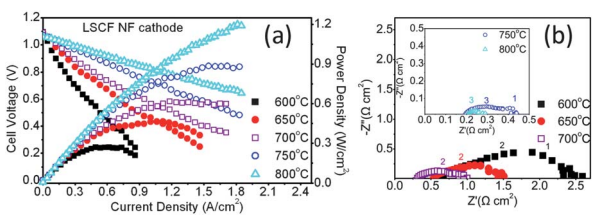

Fig. 5 (a) V–I curves and (b) impedance spectra of the fuel cells with monolithic LSCF nanofiber cathodes at different operating temperatures. The numbered labels are the logarithms of the characteristic frequencies.

at ~0.65 V at 800 °C. Our result was comparable to those for SOFCs based on the LSCF cathode with a similar configuration.[20,24–29] The cell polarization resistance was then derived from the impedance spectra in Fig. 5(b) by subtracting the contact resistance (high-frequency intercept at Z' axis) from the total resistance (low-frequency intercept at Z' axis). The fuel cell showed a large polarization resistance of 1.86 Ω cm^2 at 600 °C, which dropped to 0.26 Ω cm^2 and 0.10 Ω cm^2 at 750 °C and 800 °C, respectively. The logarithms of the characteristic frequency of the semi-arc are also labeled on the spectra. As the temperature increased, the characteristic frequency shifted to a high-frequency regime. At 750 °C, two depressed arcs were observed with characteristic frequency in the region of 10^3 and 10^1 Hz, respectively. The first arc was assigned to the charge transfer process and the second one was related to the dissociation of oxygen molecules and adsorption of oxygen gas into the cathode.[30] The detailed analysis of the impedance spectra can be found in the ESI†. It should be noted that the contact resistance was comparable to or even larger than the polarization resistance above 700 °C. Hence the *V–I* curves showed a linear shape, which indicated that the main loss was due to the IR drop.

The electrochemical performance of SOFCs largely depends on the percolation in the electrode. Based on the percolation theory, the critical density (N_c) for percolation in a random distributed "conducting stick" network can be written as[31,32]

$$l \times \sqrt{\pi N_c} = 4.236 \quad (3)$$

where l is the length of the "conducting stick". Assuming that the average length of nanofibers was 20 μm from Fig. 4(a), N_c was estimated to be ~1.5 × 10^{-2} μm^{-2}, which was much less than the observed nanofiber density. Therefore it can be concluded that the nanofiber network cathode was highly percolated and connected, which offered a "highway" for transport of both electrons and oxygen ions. Considering the oxygen reduction process in which electrons and oxygen ions need to be transported simultaneously in and out of the reaction zone, such a highly percolated and conductive structure is critical to achieving a large number of oxygen reduction reaction sites.

In short, the nanofiber network structure has several advantages: (i) a high percolation; (ii) a high porosity; and (iii) it gives a continuous pathway for charge transport. In addition, the porous nanofiber network structure is also a good scaffold for infiltration. In order to enhance the transport of oxygen ions in the cathode, GDC was infiltrated into the LSCF nanofiber cathode because GDC has been reported to have a higher coefficient of oxygen ion diffusion than LSCF.[33,34] In addition, GDC can be used tune the thermal expansion coefficient of the electrode, which benefits the sintering process.[11,29] Furthermore, addition of GDC into LSCF could significantly reduce the electrode polarization resistance. Also, the optimized GDC ratio has been reported to be 36–60 wt% depending on the cathode microstructures and the fabrication process.[5,34–37] Therefore, 20 wt% and 50 wt% (relative to the whole cathode mass after infiltration) GDC was infiltrated into the nanofiber cathode using nitrate precursor and subsequent heating. The corresponding fuel cells are denoted in the following as LSCF20GDC and LSCF50GDC, respectively.

Fig. 6 shows the *V–I* curves and the impedance spectra obtained from the fuel cells with the LSCF–GDC composite

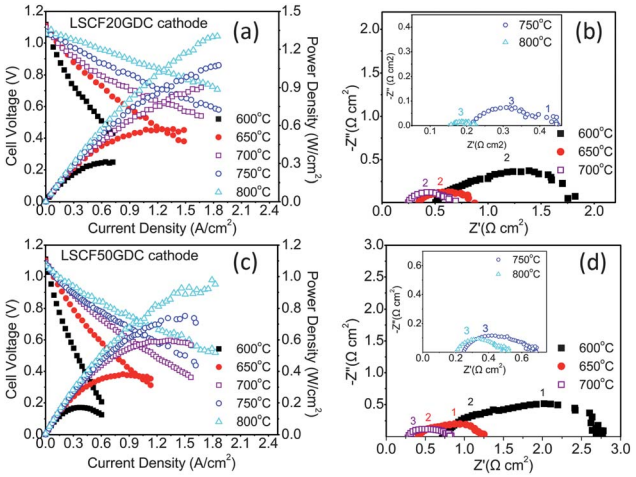

Fig. 6 (a) *V–I* curves and (b) impedance spectra of the fuel cell (LSCF20GDC) with the LSCF–20% GDC composite cathode at different operating temperatures; (c) *V–I* curves and (d) impedance spectra of the fuel cell (LSCF50GDC) with the LSCF–50% GDC composite cathode.

cathode. It can be seen that the power densities of the LSCF20GDC cell at all testing temperatures were higher than those of the corresponding monolithic LSCF NF cell. The highest power densities were 0.31 W cm^{-2} and 1.33 W cm^{-2} at 600 °C and 800 °C, respectively. At 750 °C, the power density (1.07 W cm^{-2} at 1.90 A cm^{-2}) was about 19% greater than that of the LSCF NF cell (0.90 W cm^{-2} at 1.90 A cm^{-2}), which reveals that the 20 wt% GDC infiltration effectively improved the performance of the nanofiber cathode, especially at the intermediate temperature. The polarization resistance of the LSCF20GDC cell was reduced to 0.21 Ω cm^2 at 750 °C as compared to that of the LSCF NF cell (0.26 Ω cm^2). However, the performance deteriorated when the amount of GDC increased to 50 wt%. A power density of only 0.79 W cm^{-2} was recorded at 1.47 A cm^{-2} at 750 °C, which was 17% lower than that of the LSCF NF cell. Such performance degradation is also reflected by the impedance spectra in Fig. 6(d), which show that the polarization resistance of the fuel cell increased remarkably to 0.45 Ω cm^2 with the overloaded GDC. This was roughly two times higher than that of the monolithic LSCF NF cell. A detailed fitting process of impedance spectra is seen in the ESI (Fig. S1†). It was found that infiltrating 20 wt% of GDC slightly increased the contact resistance of the cell but had little effect on the charge transfer resistance. The oxygen dissociation and adsorption resistance was reduced. In contrast, the contact resistance in the LSCF50GDC cell obviously increased, and the oxygen dissociation and adsorption resistance significantly increased.

In order to clarify the difference in the performance of the SOFCs with different amounts of infiltrated GDC, the microstructures of the cathodes were examined. Fig. 7 shows the surface morphology of the LSCF–GDC composite cathodes. After addition of 20 wt% GDC into the LSCF cathode, the porous nanofiber network structure was retained (Fig. 7(a and b)). There was no noticeable change in the length of the nanofibers. The mean diameter of the nanofiber increased to 340 nm. GDC was

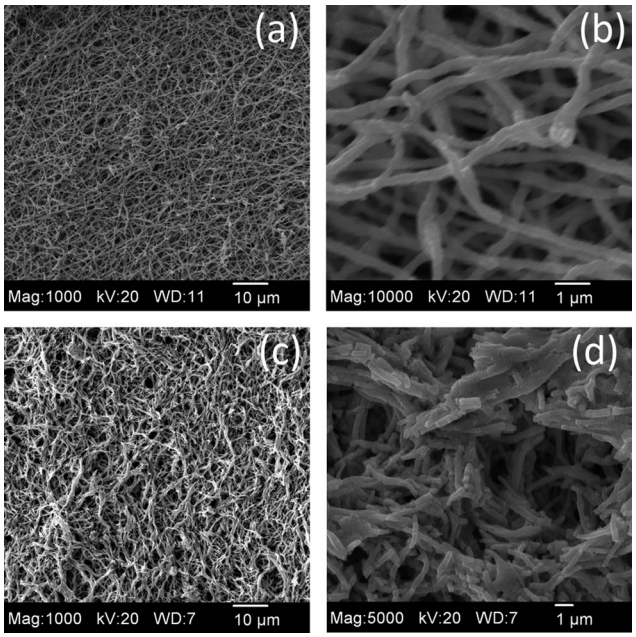

Fig. 7 SEM images of the GDC-infiltrated LSCF nanofiber cathode; (a) and (b) the LSCF–20% GDC cathode at low and high magnification, respectively; (c) and (d) LSCF–50% GDC cathode at low and high magnification, respectively.

observed to be coated on the surface of the LSCF nanofibers rather than to be filled into the network pores between the nanofibers, which allowed the porosity of the network to remain high. The TEM image also revealed that the coated GDC actually formed nanoparticles of about 30 nm in size on the LSCF nanofiber surface (Fig. S3†). It should be noted that such a porous coating allowed for open access of oxygen molecules to the LSCF catalyst, and facilitated ion transport in the cathode. Therefore, the LSCF20GDC composite cathode exhibited higher power density. Additional SEM image and EDX spectra are shown in Fig. S2†. In contrast, after addition of 50 wt% GDC into the LSCF cathode, the nanofibers were broken, leading to the reduction of the fiber length to 5–10 μm. In addition, many short fibers were embedded in the large GDC aggregates (Fig. 7(d)), which was confirmed by EDX analysis (Fig. S4†). As a result, the charge-transport pathway became disconnected and the percolation of the nanofiber network was affected. Furthermore, the porosity of the cathode was also reduced as the overloaded GDC appeared at the intersections of the LSCF nanofiber network. It can be seen from the TEM images (Fig. S5†) that a large amount of film-like GDC was present between the nanofibers. The thick GDC coating may block the gas/catalyst interface, which resulted in larger gas adsorption and dissociation resistance in the impedance spectrum. Therefore it was not surprising that the performance of the LSCF50GDC cell was worse than that of the LSCF20GDC cell.

The stability of the cathodes was examined under operating conditions. Fig. 8 shows XRD plots of the cathodes after electrochemical testing of the SOFC cells. The XRD pattern of the bare half-cell can be indexed as fluorite ceria, which came from the buffer layer of GDC. The peak intensity was consistent with the relative cathode composition, which indicated the chemical

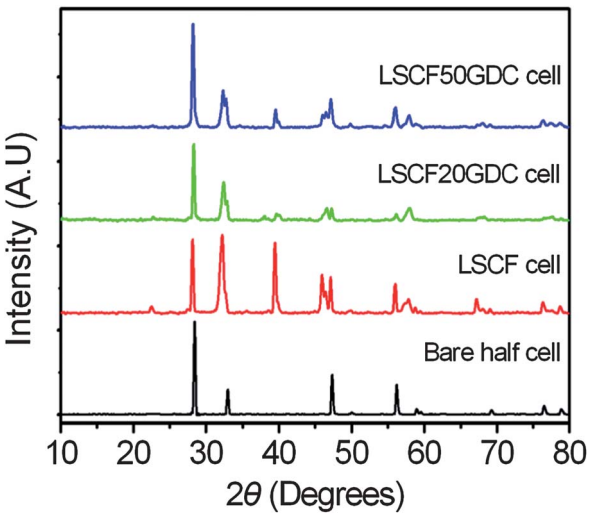

Fig. 8 XRD patterns of the cathodes taken after testing of the fuel cells.

integrity. In particular, all the cathodes contained a mixture of LSCF and GDC phases without any other impurity. This means that the GDC buffer layer successfully prevented the interaction of LSCF with YSZ at high temperature. In addition, the fuel cell with the monolithic LSCF nanofiber cathode was operated at different current loadings at 750 °C for 200 h in order to test the stability of the electrochemical performance (Fig. 9). The power density dropped 5% after the first 25 h of operation at a loading of 0.5 A cm^{-2}. The degradation rate was 7% at 0.25 A cm^{-2} for 100 h. After the current loading was switched back to 0.5 A cm^{-2}, the fuel cell eventually became stable during operation for an additional 60 h. After stability testing, the fibrous structure of the cathode was retained, as shown in Fig. S6†. It is unclear why the performance of the fuel cell was degraded for the first 25 h. It may be attributed to the interaction between the electrode and the electrolyte or to the Sr chemical migration reported in ref. 38.

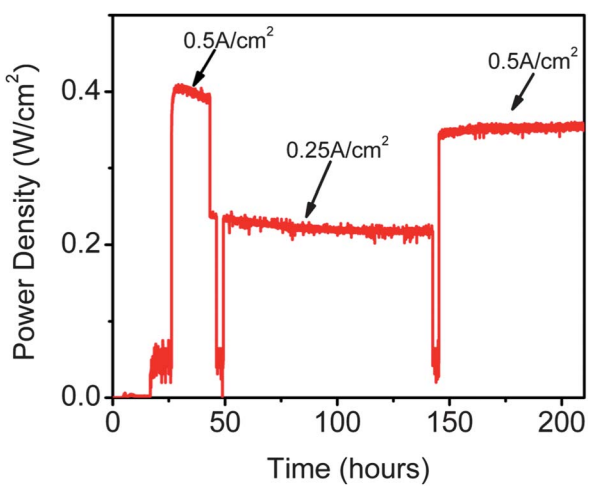

Fig. 9 Power output of the fuel cell with monolithic LSCF nanofiber cathode tested at 750 °C for 200 h.

4. Conclusions

LSCF nanofibers were successfully synthesized by electrospinning processing and used for SOFC cathodes that were targeted for operation at intermediate temperature. The results showed that the nanofiber architecture was stable at intermediate operating temperature. The LSCF nanofibers were interconnected with each other to form a highly porous network structure. Such a nanofiber network provided continuous pathways for charge transport throughout the cathode. In addition, high percolation was observed in the nanofiber cathode. The fuel cell with a monolithic LSCF nanofiber cathode exhibited a power density of 0.90 W cm^{-2} at 1.9 A cm^{-2} at 750 °C. The electrochemical performance of the fuel cell was further improved by infiltration of 20 wt% of GDC into the LSCF nanofiber scaffold. The fuel cell with the LSCF–20%GDC composite cathode showed a power density of 1.07 W cm^{-2} at 750 °C. Excessive infiltration of GDC degraded the performance of the SOFC. The present work shows that the performance of intermediate-temperature SOFCs can be improved by engineering the electrode architecture on the nanoscale.

Acknowledgements

This work was supported by the National Energy Technology Laboratory's on-going research in fuel cell project DE-FE0000400 under the URS Corporation contract and West Virginia State Research Challenge Grant Energy Materials Program (EPS08-01). The authors are grateful for the helpful discussion with Dr Kirk Gerdes at NETL and Fanke Meng and Savan Suri at WVU for characterization assistance.

Notes and references

1 Q. N. Minh, *J. Am. Ceram. Soc.*, 1993, **76**, 563–588.
2 T. Suzuki, M. Awano, P. Jasinski, V. Petrovsky and H. U. Anderson, *Solid State Ionics*, 2006, **177**, 2071–2074.
3 M. J. Zhi, X. Chen, H. Finklea, I. Celik and N. Q. Wu, *J. Power Sources*, 2008, **183**, 485–490.
4 F. N. Cayan, M. J. Zhi, S. R. Pakalapati, I. Celik, N. Q. Wu and R. Gemmen, *J. Power Sources*, 2008, **185**, 595–602.
5 Z. Y. Jiang, C. R. Xiang and F. L. Chen, *Electrochim. Acta*, 2010, **55**, 3595–3605.
6 A. Tarancón, *Energies*, 2009, **2**, 1130–1150.
7 C. W. Sun, R. Hui and J. Roller, *J. Solid State Electrochem.*, 2010, **14**, 1125–1144.
8 J. Wang, A. Manivannan and N. Q. Wu, *Thin Solid Films*, 2008, **517**, 582–587.
9 M. J. Zhi, G. W. Zhou, Z. L. Hong, J. Wang, R. Gemmen, K. Gerdes, A. Manivannan, D. L. Ma and N. Q. Wu, *Energy Environ. Sci.*, 2011, **4**, 139–144.
10 M. G. Bellino, J. G. Sacanell, D. G. Lamas, A. G. Leyva and N. E. Walsöe de Reca, *J. Am. Chem. Soc.*, 2007, **129**, 3066–3067.
11 M. E. Lynch, L. Yang, W. T. Qin, J. J. Choi, M. F. Liu, K. Blinn and M. L. Liu, *Energy Environ. Sci.*, 2011, **4**, 2249–2258.
12 E. Mutoro, E. J. Crumlin, M. D. Biegalski, H. M. Christen and Y. Shao-Horn, *Energy Environ. Sci.*, 2011, **4**, 3689–3696.
13 S. Cavaliere, S. Subianto, I. Savych, D. J. Jones and J. Rozière, *Energy Environ. Sci.*, 2011, **4**, 4761–4785.
14 A. Mai, V. A. C. Haanappel, S. Uhlenbruck, F. Tietz and D. Stöver, *Solid State Ionics*, 2005, **176**, 1341–1350.
15 Y. Huang, J. M. Vohs and R. J. Gorte, *Electrochem. Solid-State Lett.*, 2006, **9**, A237–A240.
16 T. Z. Sholklapper, V. Radmilovic, C. P. Jacobson, S. J. Visco and L. C. De Jonghe, *Electrochem. Solid-State Lett.*, 2007, **10**, B74–B76.
17 M. J. Zhi, N. Mariani, R. Gemmen, K. Gerdes and N. Q. Wu, *Energy Environ. Sci.*, 2011, **4**, 417–420.
18 C. Jiang, F. Wang, N. Q. Wu and X. G. Liu, *Adv. Mater.*, 2008, **20**, 4826–4829.
19 N. Q. Wu, J. Wang, D. Tafen, H. Wang, J. G. Zheng, J. P. Lewis, X. G. Liu, S. S. Leonard and A. Manivannan, *J. Am. Chem. Soc.*, 2010, **132**, 6679–6685.
20 F. C. Fonseca, S. Uhlenbruck, R. Nedéléc and H. P. Buchkremer, *J. Power Sources*, 2010, **195**, 1599–1604.
21 N. H. Menzler, F. Tietz, S. Uhlenbruck, H. P. Buchkremer and D. Stöver, *J. Mater. Sci.*, 2010, **45**, 3109–3135.
22 W. A. Meulenberg, N. H. Menzler, H. P. Buchkremer and D. Stöver, *Ceram. Trans.*, 2002, **127**, 99–107.
23 B. Gut and M. Wagmann, *Proceedings of the 3rd European Solid Oxide Fuel Cell Forum*, Nantes, France, 1998, pp. 161–170.
24 F. Tietz, V. A. C. Haanappel, A. Mai, J. Mertens and D. Stöver, *J. Power Sources*, 2006, **156**, 20–22.
25 N. Jordan, W. Assenmacher, S. Uhlenbruck, V. A. C. Haanappel, H. P. Buchkremer, D. Stöver and W. Mader, *Solid State Ionics*, 2008, **179**, 919–923.
26 S. P. Simner, M. D. Anderson, M. H. Engelhard and J. W. Stevenson, *Electrochem. Solid-State Lett.*, 2006, **9**, A478–A481.
27 W. Zhou, Z. P. Shao, R. Ran, H. X. Gu, W. Q. Jin and N. P. Xu, *J. Am. Ceram. Soc.*, 2008, **91**, 1155–1162.
28 Y. Sakito, A. Hirano, N. Imanishi, Y. Takeda, O. Yamamoto and Y. Liu, *J. Power Sources*, 2008, **182**, 476–481.
29 Y. Sakito, A. Hirano, N. Imanishi, Y. Takeda, O. Yamamoto, Y. Liu and M. Mori, *J. Fuel Cell Sci. Technol.*, 2008, **5**, 2008–2011.
30 S. W. Lee, N. Miller, M. Staruch, K. Gerdes, M. Jain and A. Manivannan, *Electrochim. Acta*, 2011, **56**, 9904–9909.
31 H. Wu, L. B. Hu, M. W. Rowell, D. S. Kong, J. J. Cha, J. R. McDonough, J. Zhu, Y. Yang, M. D. McGehee and Y. Cui, *Nano Lett.*, 2010, **10**, 4242–4248.
32 L. Hu, D. S. Hecht and G. Grune, *Nano Lett.*, 2004, **4**, 2513–2517.
33 P. E. Murray, M. J. Sever and S. Barnett, *Solid State Ionics*, 2002, **142**, 27–34.
34 R. Doshi, V. L. Richards, J. D. Carter, X. P. Wang and M. Krumpelta, *J. Electrochem. Soc.*, 1999, **146**, 1273–1278.
35 H. J. Hwang, J. W. Moon, S. Lee and E. A. Lee, *J. Power Sources*, 2005, **145**, 243–248.
36 Y. J. Leng, S. H. Chan and Q. Liu, *Int. J. Hydrogen Energy*, 2008, **33**, 3308–3317.
37 I. Kim, S. Barnett, Y. Jiang, M. Pillai, N. McDonald, D. Gostovic, Z. Zhan and J. Liu, Final Report to DoE Award DE-FC26-02NT41570, 2008.
38 S. P. Simner, M. D. Anderson, M. H. Engelhard and J. W. Stevenson, *Electrochem. Solid-State Lett.*, 2006, **9**, A478–A481.